UNIVERSITY OF LATVIA

Summary of Doctoral Thesis

Aleksandrs Platoņenko

FIRST PRINCIPLES MODELLING AND CHARACTERIZATION OF RADIATION POINT DEFECTS IN α-Al_2O_3 AND $MgAl_2O_4$ CRYSTALS

Riga 2023

UNIVERSITY OF LATVIA

FACULTY OF PHYSICS, MATHEMATICS AND OPTOMETRY

Aleksandrs Platoņenko

FIRST PRINCIPLES MODELLING AND CHARACTERIZATION OF RADIATION POINT DEFECTS IN α-Al_2O_3 AND $MgAl_2O_4$ CRYSTALS

SUMMARY OF DOCTORAL THESIS

Submitted for the Doctoral degree in physics
subfield of physics, astronomy and mechanics

Riga 2023

The doctoral thesis was carried out at the Institute of Solid State Physics, University of Latvia from 2014 to 2023.

The doctoral thesis contains the introduction and eight scientific publications. Form of the doctoral thesis: collection of publications in Physics and Astronomy, subfield of solid state physics.

Supervisor:
Dr. rer. nat. **Deniss Grjaznovs**, leading researcher of Laboratory of Kinetics in Self-Organizing Systems at Institute of Solid State Physics, University of Latvia.

Reviewers:

1) Prof. Dr. **Theo Scherer**, Karlsruhe Institute of Technology (Germany);
2) Dr. phys. **Andris Guļāns**, University of Latvia;
3) Dr. phys. **Mikhail Brik**, Tartu Universtity (Estonia).

The thesis will be defended at the public session Doctoral Committee of Physics, Astronomy and Mechanics, University of Latvia, at 15:00 on May 19, 2023, in the conference hall of the Institute of Solid State Physics of University of Latvia.

The thesis is available at the Library of the University of Latvia, Kalpaka blvd. 4.

Chairman of the Doctoral Committee — Dr. habil. phys. Linards Skuja

Secretary of the Doctoral Committee — Sintija Siliņa

ISBN 978-9934-18-983-8
ISBN 978-9934-18-984-5 (PDF)

ABSTRACT

Corundum (α–Al_2O_3) and Mg–Al spinel ($MgAl_2O_4$) have high radiation stability, which makes them promising materials for high-energy nuclear technologies and future fusion reactors as a protective coating to avoid the light gases permeation, as well as corrosion produced by lithium-based alloys.

Despite the wide application and importance of these materials, the structure of the corresponding point defects is still not well studied from a theoretical point of view. Radiation-induced changes in the structural and optical properties of corundum are mainly associated with oxygen vacancies and complementary Frenkel pair defects (vacancy + interstitial oxygen atom). While oxygen vacancies are well-studied and easily identified, the complementary defect – the interstitial oxygen atom – has not been described in detail both experimentally and theoretically until now. The situation is similar for spinel crystals, as well another range of defects appears there – antisite defects, which also play an important role in the radiation resistance of the material.

Using quantum mechanical modelling code CRYSTAL17, which is based on the Density Functional Theory (DFT) and Linear Combination of Atomic Orbitals (LCAO), radiation defects in α–Al_2O_3 structure were investigated: both F-centers and interstitial oxygen defects in different charge states. The charge distribution in the Al and O sublattices, the defect geometry, as well as the recombination energy barrier, which characterizes the stability of primary defects, were analyzed. The application of Raman spectroscopy for defect identification was also proposed. The recombination energy barrier of the oxygen defect in $MgAl_2O_4$ was determined, as well as the EPR parameters of various antisite and vacancy defect (V-centers) of individual cations were calculated.

An efficient comparison of the calculated and experimental results allowed a deeper understanding of the behavior of Al_2O_3 and $MgAl_2O_4$ point defects, which can also be applied to the entire range of oxide materials.

LIST OF ABBREVATIONS

0D	zero-dimensional
1D	one-dimoensional
2D	two-dimensional
3D	three-dimensional
ADP	anisotropic displacements parameter
DFT	density functional theory
dpa	displasment per atom
DRC	distinguished reaction coordinate
EPR	electronic paramagnetic resonanse
HFS	hyperfine structure
LCAO	linear combination of atomic orbitals,
SHI	switft heavy ion
TDE	threshold displacement energy
VUV	vacuum ultraviolet
XC	exchange-corelation functional

CONTENTS

ABSTRACT 3

LIST OF ABBREVATIONS 4

1. INTRODUCTION 6

1.1. Motivation 6

1.2. Author's contribution 7

1.3. Scientific novelty 8

2. LITERATURE REVIEW 9

2.1. Radiation-induced changes in crystalline materials 9

2.2. Radiation resistance of α–Al_2O_3 11

2.3. Radiation resistance of $MgAl_2O_4$ 12

3. FIRST PRINCIPLE CALCULATIONS WITH CRYSTAL17 CODE 14

3.1. General information 14

3.2. Calculation methods of various properties 15

3.2.1. Defect modelling 15

3.2.2. Calculations of the migration barrier 16

3.2.3. Vibrational properties 17

3.3.2. Model and calculation parameters selection 18

4. MAIN RESULTS 19

4.1. Oxygen interstitial defects structure and properties 19

4.2. Migration of oxygen interstitial defects in the crystal lattice 22

4.2.1. α–Al_2O_3 22

4.2.2. $MgAl_2O_4$ 24

4.3. $MgAl_2O_4$ antisite defects properties and EPR parameters calculations 25

4.4. Vibrational modes induced by point defects in α–Al_2O_3 crystals 27

5. SUMMARY 29

6. MAIN THESES 30

7. LITERATURE 31

7.1. Author's publications related to this work 31

7.2. Other author's publications 31

7.3. References 33

8. ACKNOWLEDGEMENTS 39

1. INTRODUCTION

1.1. Motivation

Wide-bandgap oxides such as MgO, α–Al_2O_3 (corundum), $MgAl_2O_4$ (spinel) are considered promising materials for diagnostic and optical components in nuclear fusion devices. The accumulation of radiation-induced defects affects the optical and other properties of the components. Thus, understanding the defect stability and recombination mechanisms becomes a very important issue. It is generally accepted that the radiation resistance of functional materials is mainly determined by the accumulation of primary structural defects – vacancies + interstitial atoms, or Frenkel pairs. In the more complex structure of spinel, another stabilizing mechanism appears – antisite defects.

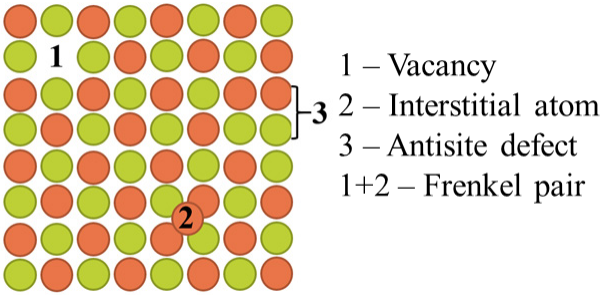

Figure 1.1. Crystal point defects, which were discussed in the thesis.

All such defects were mostly studied with optical methods – they are widely available and allow for obtaining almost all the necessary information about the formation and evolution of the defects. However, for a long time, only vacancy defects were observed in experiments, with the interstitial atoms remaining invisible. Later, oxygen interstitial defects were detected in MgO, CaO, SrO and ZnO by EPR method.

Therefore, the main goals of this thesis are to understand the properties of oxygen defects in α–Al_2O_3 and $MgAl_2O_4$ crystals, to look at the properties of antisite defects, as well as to propose their possible non-optical detection methods. To achieve these goals, the following tasks were set:

- Modeling of pristine crystals to select optimal calculation parameters that well describe the mechanical and electronic properties of crystals.
- Calculations of interstitial oxygen defects in different charge states (+1, 0, –1), analysis of their properties.

- Modeling of migration of interstitial oxygen defect in Al_2O_3 and $MgAl_2O_4$ crystals.
- Modeling of antisite defects in $MgAl_2O_4$ crystals.
- Calculations of vacancy defects (or F-centers) and their dimers, determining their vibrational properties and simulating Raman spectra.

The work was performed within the framework of the EUROFUSION project (Enabling research and WP–MAT sub-projects), where scientists from other countries also participated, who conducted experimental research on these materials.

1.2. Author's contribution

The results described in this thesis have been summarized in eight high-ranking international publications [P1–P8] and were also presented at several local and international conferences with poster and oral presentations. The author has performed all calculations and their processing, was the responsible author for three publications, and played a significant role in writing all publications, as well as preparing conference abstracts and presentations. Two more methodological articles on point defects modeling are not included in this thesis [A1, A2]. Since 2016, the author has been acquiring computational resources at HELIOS (Japan) and CINECA-MARCONI (Italy) supercomputers, writing applications and reports on the use of resources. During the development of the work, the author has attended three international summer schools.

[P1] **Platonenko, A**., Piskunov, S., Zhukovskii, Y. F., Kotomin, E. A., *Ab initio* simulations on Frenkel pairs of radiation defects in corundum, IOP Conference Series: Materials Science and Engineering, **77 (1)** (2015): 012001. IF = 0.53 (50% of the planning and writing; all calculations presented in the paper, corresponding author responsibility)

[P2] Zhukovskii, Y. F., **Platonenko, A.,** Piskunov, S., Kotomin, E. A., *Ab initio* simulations on migration paths of interstitial oxygen in corundum, Nuclear Instruments and Methods in Physics Research, Section B: Beam Interactions with Materials and Atoms, **374** (2016): 29–34. IF = 1.27 (70% of the planning and writing; all calculations presented in the paper)

[P3] **Platonenko, A.,** Gryaznov, D., Piskunov, S., Zhukovskii, Y. F., Kotomin, E. A., Charged oxygen interstitials in corundum: first principles simulations, Physica Status Solidi (C) Current Topics in Solid State Physics, **13** (10–12) (2016): 932–936. IF = 0.81 (75% of the planning and writing; all calculations presented in the paper, corresponding author responsibility)

[P4] **Platonenko, A.,** Gryaznov, D., Zhukovskii, Y. F., Kotomin, E. A., *Ab initio* simulations on charged interstitial oxygen migration in corundum, Nuclear Instruments and Methods in Physics Research, Section B: Beam

Interactions with Materials and Atoms, **435** (2018): 74–78. IF = 1.27 (75% of the planning and writing; all calculations presented in the paper, submission preparation)

[P5] **Platonenko, A.,** Gryaznov, D., Zhukovskii, Y. F., Kotomin, E. A., First Principles Simulations on Migration Paths of Oxygen Interstitials in $MgAl_2O_4$, Physica Status Solidi (B) Basic Research, **256** (5) (2019): 1800282. IF = 1.48 (75% of the planning and writing; all calculations presented in the paper, submission preparation)

[P6] **Platonenko, A.,** Gryaznov, D., Kotomin, E. A., Lushchik, A., Seeman, V., Popov, A. I., Hybrid density functional calculations of hyperfine coupling tensor for hole-type defects in $MgAl_2O_4$, Nuclear Instruments and Methods in Physics Research, Section B: Beam Interactions with Materials and Atoms, **464** (2020): 60–64. IF = 1.27 (50% of the planning and writing; most calculations presented in the paper)

[P7] Seeman, V., Lushchik, A., Shablonin, E., Prieditis, G., Gryaznov, D., **Platonenko, A.,** Kotomin, E. A., Popov, A. I., Atomic, electronic and magnetic structure of an oxygen interstitial in neutron-irradiated Al2O3 single crystals, Scientific Reports, **10** (2020): 15852. IF = 4.58 (50% of the planning and writing of theoretical part of the paper; all *ab initio* calculations presented in the paper)

[P8] **Platonenko, A.,** Gryaznov, D. Popov, A. I., Dovesi, R., Kotomin, E. A., First principles calculations of the vibrational properties of single and dimer F-type centers in corundum crystals, Journal of Chemical Physics, **153** (2020): 134107. IF = 2.99 (80% of the planning and writing; all calculations presented in the paper, corresponding author responsibility)

1.3. Scientific novelty

The author's articles described for the first time the properties of oxygen interstitial defects and their migration in the crystal lattice, using large-scale models for calculations and applying advanced hybrid density functionals. It is shown that the oxygen interstitial defect can exist in different forms in both Al_2O_3 and $MgAl_2O_4$. These results were used to describe experimental observations in Al_2O_3 crystals.

Calculations of antisite defects (V-centers) in $MgAl_2O_4$ helped verify experimental observations.

For the first time, defect-induced vibrational modes have been calculated and demonstrated, which could be used to detect defects under conditions where optical measurements are not possible.

2. LITERATURE REVIEW

2.1. Radiation-induced changes in crystalline materials

Particles with energy well above normal thermal energy (E_{kin} > 1 eV) exist in nature as cosmic rays or as a product of radioactive decay, but nowadays they are also artificially produced for scientific [1, 2] and practical purposes [3, 4].

The interaction of materials with high-energy particles results in the formation of defects when the kinetic energy of the particles is transferred to the atoms. In parallel with this, various electronic processes (excitation, generation of excitons and plasmons) and heating of the material can take place. The simplest defect that can form in all materials is a vacancy (V) and an interstitial atom (I), which are also called a Frenkel pair: when an atom is knocked out of its regular position, leaving behind a vacancy, but itself occupies a place in the lattice between other atoms [5]. Namely, more complex defects can also form: voids, amorphous regions, dislocations, defect clusters. The range of possible defects also depends on the type of compound: while only one type of V + I pair is possible in metals, oxides, where there are two types of atoms, will have both anionic and cationic defects. As well, in wide-band materials, electron localization in anion vacancies is possible [6].

Damage to the material under the influence of high-energy particles occurs in two stages: as a result of a primary particle-atom collision, when the kinetic energy of the particle dissipates in a cascade of collisions, due to which the material heats up strongly and the system is far from thermodynamic equilibrium. The second stage is the thermalization process, when the system comes to equilibrium. the duration of the first stage depends on the particle energy and temperature (shorter at higher temperatures), but is usually < 1 ps, but thermalization lasts up to 10 ps [5, 7].

Threshold displacement energy (TDE) is an important parameter for characterizing radiation damage. It is the amount of energy that is needed to knock an atom out of its equilibrium state and create a stable defect [8]. The possibility of defect formation below this energy is zero, but increases rapidly above it. Assuming that only one atom moves as a result of the collision and determining the potential energy barrier along a straight line in the direction of the initial recoil, it becomes clear that the threshold displacement energy will depend on the orientation of the crystal. But this is a very simplified view of what happens after a high-energy particle collides with a crystal atom. In a crystal, each crystallographic direction corresponds to a separate displacement threshold energy [8].

The displacement threshold energy is determined both experimentally and with the help of simulations [9, 10]. Simulations were usually based on

pair-potential molecular dynamics, but recently *ab initio* molecular dynamics is becoming increasingly popular.

Knowing how many and which stable defects will form as a result of irradiation, the radiation resistance of the material can be roughly estimated. The radiation resistance of metals has been studied since the middle of the last century, mainly trying to find out the effect of neutrons on the structural parts of nuclear reactors. Metals are very well described by classical molecular dynamics and relatively simple mathematical models (e.g. the Norgett, Robinson and Torrens (NRT) equation [11]), and experimental defect detection with *in situ* resistance measurements at low temperatures is very accurate and common [12]. Consequently, the level of understanding of radiation damage in metals is also the highest among all classes of materials [13].

Research on the radiation resistance of oxides has lagged behind that of metals for a long time, but is becoming increasingly relevant. The average value of TDE in oxides is between ∼40 and ∼100 eV, which is larger than in metals. In addition, only 20–50% of the defects predicted by NRT calculations in a wide radiation energy range are formed in oxides [14, 15]. Optical methods, electron magnetic resonance dominate among the available defect detection methods, but they are applicable only to a part of all defects, while defect clusters that do not have an optical or EPR signal remain invisible. One method that could help is, for example, small angle neutron scattering [16], but it is not so widely available.

Oxide materials are used in environments with high-energy radiation as functional materials (in components of diagnostic or optical devices) [17, 18], so it is important not only how their mechanical properties change, as might be the case for structural materials, but also to monitor the changes in optical, electronic and other properties. The efficiency of radiation damage in wide-bandgap (> 6 eV) metal oxides, which are characterized by a rather high Frenkel defect pair formation energy (significantly greater than the forbidden gap E_g), is highly dependent on the type of radiation. For example, ordinary X-rays and γ-rays do not create new structural defects in metal oxides, but only charge already existing defects and impurities by induced charge transfer. Meanwhile, in other ionic materials – alkali metal halides – defects can form even under intense VUV radiation [19]. Using the ionization mechanism, a Frenkel pair is formed, the formation energy of which is lower than the band gap, as a result of the decay of an exciton of a non-radiative localized anion or as a result of the relaxation of an electron-hole pair [20]. When irradiating metal oxides with swift heavy ions (SHI), a large part of the energy is dissipated in the ionization processes that take place around the heavy ion in the crystal. It was shown that radiation damage is not significantly different in the results of neutron and SHI irradiation, so it was concluded that electronic excitation mechanisms only have a small effect on the formation of radiation defects [21, 22].

2.2. Radiation resistance of α–Al_2O_3

α–Al_2O_3 (corundum, sapphire) is a promising material for fusion reactors, e.g. for components such as breeding blankets and diagnostic windows [17, 23]. Thus, it is important to understand and control its radiation damage during intense neutron irradiation. It is known that as a result of exposure to radiation, pairs of Frenkel defects appear – interstitial atoms and vacancies – in both cation and anion sublattices [24–26].

The crystal structure of α–Al_2O_3 belongs to the rhombohedral space group R–3c (No. 167) with a rhombohedral lattice containing two Al_2O_3 formula units (10 atoms) in each primitive cell [27]. The Al and O atoms occupy 4c (0 0 z) and 6e (x 0 ¼) Wyckoff positions with site symmetry S3 = C3 and S2 = C2 and one free parameter in the hexagonal syngony, respectively. The crystallographic cell contains 6 formula units (30 atoms) (Fig. 2.1).

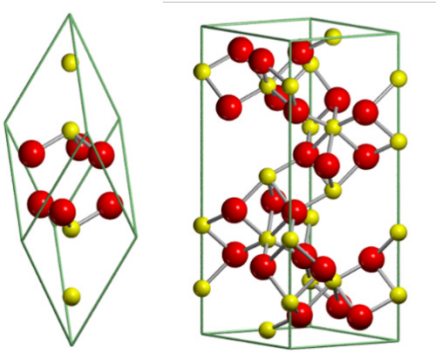

Figure 2.1. α–Al_2O_3 primitive 10-atom cell and crystallographic 30-atom unit cell.

Measured shifts in the threshold energy for corundum show that cations are more easily knocked out of the equilibrium position: 18–24 eV versus 70+ eV for anions [28, 29]. However, cationic sublattice defects do not accumulate in high concentrations [30], which is most likely due to very high defect mobility, and to observe them, irradiation and measurements at low temperatures should be performed. But since corundum is used at elevated temperatures in all radiation-related applications, cation defects do not significantly affect the properties of the material.

Anionic sublattice defects accumulated in alumina, affecting its optical and mechanical properties. The primary defect is an oxygen vacancy, where one (F^+ center) or two electrons (F center) can be localized. The F-center is characterized by a strong absorption band at 6 eV, while the F^+ center has two absorption bands: 5.3 eV and 4.8 eV [31, 32]. It should be noted that in all measurements the absorption of the F^+ center is much lower than the absorption

of the F center. Under neutron irradiation, dimers of these defects are also formed – F_2 with different number of electrons.

It is assumed that the annealing of individual F-centers in neutron-irradiated metal oxides is due to the fact that interstitial oxygen atoms become mobile at elevated temperature and recombine with still immobile anion vacancies that are part of F^+ and F centers, while thermal annealing is due to the absorption of F and F^+ of bands in doped corundum, which does not contain anionic interstitial atoms, occurs at a significantly higher temperature [33].

In contrast to electron centers, the properties of interstitial oxygen atoms have been experimentally very little studied, as they do not have pronounced magnetic properties and optical absorption in a suitable energy range. Such studies are of great importance because in most binary oxides (as well as alkali halides), oxygen/halide interstitial atoms are more mobile than complementary vacancies, and their diffusion-controlled recombination determines stable defect concentrations at moderate and high temperatures [34]

Until these, some theoretical studies from the first principles were carried out on oxygen interstitial defects in different charge states in binary metal oxides [35, 36]. Interstitial atoms have been shown to bond with the lattice regular oxygen ion MgO [37, 38] and α–Al_2O_3 [39, 40]. The description of the properties of interstitial defects in α–Al_2O_3 is limited to the electronic structure, which contributes very little to the interpretation of experimental data.

Since the seventies of the last century, oxygen interstitial defects have been recorded by EPR in various oxides MgO [41], CaO [42], SrO [43] and others. At the time of writing this work, there was no such information about α–Al_2O_3, but now we can note the work [P8], where the oxygen interstitial defect in corundum was identified by the EPR method. As well as the work that was created in parallel with this within the framework of the project, where two absorption bands characteristic of interstitial defects were identified – 5.60 eV for a charged defect and 6.53 eV for a neutral defect. Analyzing the defect annealing process, the kinetic parameters of the process were also determined [44, 45].

2.3. Radiation resistance of $MgAl_2O_4$

Magnesium aluminum spinel $MgAl_2O_4$ represents a wide class of compounds with the general structural formula $A^{2+}B^{3+}{}_2O^{2-}{}_4$. The spinel structure belongs to the *Fd3m* space symmetry group (No. 227) [46]. Cations in it are located in voids in a tetrahedrally and octahedrally coordinated state in a cubic dense packing of oxygen. The unit cell contains 56 atoms (Fig. 2.2.): 32 oxygen atoms, which form 32 octahedral and 64 octahedral voids, of which eight tetrahedral positions are occupied by A^{2+} ions, and sixteen octahedral positions are occupied by B^{3+} ions.

The crystalline structure of spinel leaves a very large degree of freedom for the arrangement of ions in the lattice: spinel can be inverted, where A and B cations change places, the stoichiometry of the forming oxides can be in a wide

range, maintaining the same structure. But in this work, only non-inverted stoichiometric 1:1 $MgAl_2O_4$ compound was considered.

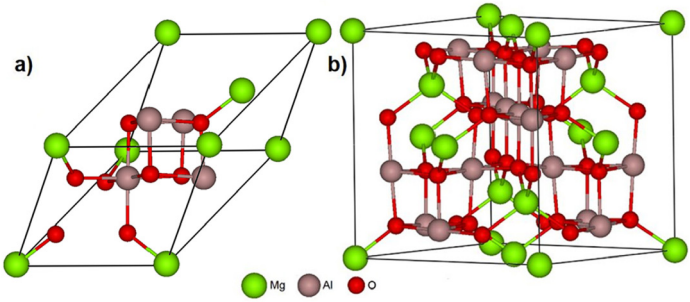

Figure 2.2. Primitive 14-atom cell (a) and crystallographic 56-atom unit cell (b).

$MgAl_2O_4$ has a very high resistance to neutron, ion and electron radiation up to extreme doses. At intense neutron irradiation [47], the spinel crystal does not change its size, while MgO and α–Al_2O_3 show volume changes > 3% even at lower doses [48]. Such a property of spinel is explained by the effective recombination process of internode and vacancy defects, which takes place during irradiation. This possibility arises because, as mentioned above, there are already many vacancies in the spinel structure that participate in recombination processes. This, in turn, leads to the formation of antibonding defects. Such defects are charged relative to the ideal lattice (+1 or –1), so they also require a charge-compensating defect nearby [49]. The concentration of antibonding defects can reach several thousand ppm, but even then, strongly defined absorption bands associated with these defects do not appear [50].

As in all oxides, oxygen vacancies are also formed in spinel, where one or two electrons can be localized (F+ and F centers, respectively) [51]. The F-center has a pronounced absorption at 5.3 eV, the absorption intensity of the F+ centers is much lower and is at 4.8 eV. While the formation and evolution of F-centers was actively studied [52, 53], the complementary defect, the internodal oxygen atom Oi, received less attention. Calculations using pair potentials [54, 55] and an ab initio approach [A2] showed that, similar to corundum, Oi forms a molecular-type pair with the lattice oxygen ion. Meanwhile, their recombination process remains unclear.

Cation vacancies are always present in spinel crystals, regardless of the method of acquisition [56, 57]. They have an absorption band at 3.1 eV, with the help of which their concentration is usually determined. During irradiation, cation vacancies form more slowly than anion vacancies [58], to make them optically or EPR active, ionizing radiation is required to promote hole localization on a neighboring oxygen ion [59].

3. FIRST PRINCIPLE CALCULATIONS WITH CRYSTAL17 CODE

3.1. General information

Quantum mechanical modeling based on density functional theory (DFT) and periodic boundary conditions is one of the most popular methods for describing and predicting the properties of various materials. In recent decades, modeling from first principles has become a standard additional tool for characterizing materials and explaining experimental data [60]. High accuracy and relatively low demands on computing resources make it much more attractive than other methods.

CRYSTAL is one of many programs for DFT calculations. Unlike other available programs for modeling solids that use the plane wave approach, CRYSTAL relies on atom-centered Gaussian-type basis sets for atomic description (LCAO), which can use both all-electron basis sets and only valence electrons with an effective nuclear pseudopotential for a simplified description of the inner electron. This method historically comes from the field of quantum chemistry and modeling of molecules, but over time it has become suitable for modeling crystalline substances as well [61].

CRYSTAL can effectively model 3D periodic systems (crystals, amorphous substances), and structures with limited periodicity: surfaces and interfaces (2D), nanotubes, nanowires and polymers (1D), as well as non-periodic (0D) molecules and nanoparticles [61].

Effective parallelization of program algorithms allows the program to be used on powerful supercomputers, realizing their full potential. As the size of the system (the number of atoms) increases, the complexity of the calculations increases quadratically, so that hundreds or even thousands of processors are used to perform large calculations in a reasonable time. The developers of the program emphasize that, in addition to high performance, it should also be ensured that the calculation accuracy remains at the same high level as the system size increases [62].

To start modeling a selected material, the user must first select two things: the basis set and the exchange-correlation (XC) functionals. The same chemical element can be in very different states (metal, ionic crystal, diamond and graphene) where the chemical bonds are very different. Different basis sets are developed to describe each case more precisely. A minimal atomic basis set will contain only filled electron orbitals – 1s in the case of a hydrogen atom, 1s2s2p – for an oxygen atom. To describe hybridization of orbitals and other processes related to the formation of chemical bonds, additional orbitals are added to the basis set. The larger the number of orbitals and associated functions, the more complicated the calculation will be. Basis sets for solid

state calculations can be found on the website of the CRYSTAL developers [63]. There are also attempts to develop universal basis sets [64], as well as methods to optimize and adapt existing basis sets for a specific task [65]. It should be mentioned that despite the fact that there are a lot of basis sets for molecular calculations, most of them cannot be used for calculations of periodic systems.

Today, the number of exchange-correlation functionals is around a few hundred. Some are used very rarely and only for specific tasks, while others such as PBE [66] and B3LYP [67, 68] became the main choice for a wide variety of problems. Choosing XC functionally looks at how well it reproduces properties of interest, mainly forbidden zone width and lattice parameters. In recent decades, hybrid XCs have been preferred, where part of the exchange energy is replaced by the Hartree-Fock energy, which gives better results for the description of many properties. There is an opinion that the choice of functional is largely a personal choice and the evaluation of the effectiveness of different XCs depends on the chosen statistical indicators [61].

The user should always know which properties can be obtained from DFT calculations, which will require additional calculations but for which completely different methods need to be used. From a standard calculation (with geometry optimization) with the CRYSTAL program, without additional resources, we obtain:

- The total energy of the system;
- Equilibrium positions of atoms;
- Atomic force gradients;
- Band gap;
- Atomic charges;
- Hyperfine electron-nuclear spin interaction parameters (for spin polarized systems).

Using the calculated wave function, one can further calculate the band structure, density of states diagrams, charge distribution maps and others. It should be remembered that some interactions cannot be obtained from classical and hybrid DFT. For example, relativistic effects and related processes such as spin-orbit coupling cannot be calculated if they are not explicitly included in the chosen calculation method, another example is the evaluation of weak atom-atom dispersion forces, where an additional Grimme correction must be used [69].

3.2. Calculation methods of various properties

3.2.1. Defect modelling

To model isolated defects under periodic Born-Karman boundary conditions, the model size must be such that periodic spatially repeating defects do not interact with each other. The larger the defective supercell, the smaller their interaction, but the calculation time increases with the model size. Work

[P2] showed that the properties of neutral interstitial oxygen defects in Al_2O_3 crystals do not differ in 120-atom and 270-atom cells, so a 120-atom supercell was used to model these defects in all works. Supercells up to 448 atoms were tested for $MgAl_2O_4$ calculations [P6]. A 270-atom supercell was used for vibrational property calculations in Al_2O_3 crystals of F and F_2 centers to achieve a relatively small concentration of F_2 defects..

The defect formation energy was calculated according to the equation:

$$E_f = E_D^q - E_0 - \sum_i n_i\mu_i + q(E_F + E_{VBM} + V) + E_{corr}^q \quad (3.1)$$

where E_D^q and E_0 are the total energy for a supercell with a defect in charge state q and the total energy for an ideal supercell, n_i is the number of atoms added or removed (n = –1 in the case of a vacancy), μ_i is the chemical potential of the element. E_F and E_{VBM} are the Fermi energy and valence band peak energy, V is the electrostatic potential equalization between supercells with and without defect. E_{corr}^q is the correction required in charged defect calculations to account for interactions between periodically spaced point charges[70]. It should be mentioned that in order to perform calculations of the charged systems, the CRYSTAL17 program adds a compensating "background" charge so that the calculated system is not infinitely charged.

3.2.2. Calculations of the migration barrier

The migration barrier is the energy required for an atom to reach another position in the crystal lattice. Migration takes place in the direction of the complementary defect, so when two defects meet, they recombine. The calculations in this work are based on some assumptions:

1) Defects are located at a great distance and do not "feel" each other;
2) A moving defect is O_i, because more energy is required to move the vacancy.

The "Distinguished Reaction Coordinate" (DRC) method was used to build a reaction coordinate diagrams and determine the migration barrier [71]. Finding the energy barrier with this method requires scanning calculations along the internal coordinate governing the reaction. In this case, the "reaction" can be described as the breaking of the O_i–O_{reg0} bond and the formation of a new O_i–O_{reg1} bond. This scan calculation changes the selected internal coordinate stepwise and in a controlled manner to move from the initial state to the final state, crossing the point of maximum energy. That the internal coordinate is used O_i–O_{reg1} distance, in this way every step it decreases, and O_i–O_{reg0} increases. The migration is considered complete when O_i reaches the same characteristics as at the starting point.

To test the method, a calculation was made for the interstitial oxygen defect in magnesium oxide. The cubic structure makes this material an ideal option for

approbation of methods. The determined migration barrier is 1.4 eV (Fig. 3.1.), which agrees well with experimental observations [72].

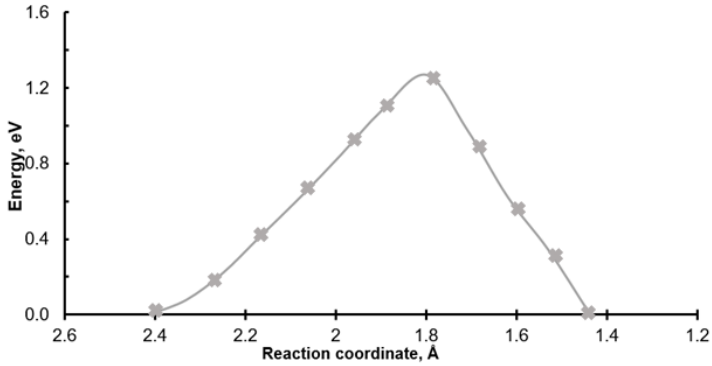

Figure 3.1. Reaction coordinate diagram for interstitial oxygen atom migration in MgO. The calculation was performed in a 64-atom supercell.

3.2.3. Vibrational properties

The vibrational frequencies at the gamma-point are obtained within the harmonic approximation [73, 74] by diagonalizing the mass-weighted Hessian matrix, the elements of which are defined as:

$$W^{\Gamma}_{\alpha i,\beta i} = \frac{H^{0}_{\alpha i,\beta i}}{\sqrt{M_{\alpha} M_{\beta}}} \tag{3.2}$$

where M_{α} and M_{β} are the masses of the atoms associated with the coordinates of atoms *i* and *j*. The first derivatives of the energy with respect to atomic positions are calculated analytically for all coordinates, while the second derivatives are calculated numerically using one shift along each coordinate for each atom. The increase in energy at displacement calculations is $\sim 10^{-5}$–10^{-7} Hartree, therefore these calculations should be performed with the qualitatively optimized geometry and increased accuracy. This is one of the more time consuming calculations as it requires N * 3 full energy calculations where N is the number of atoms in the cell (symmetric)

The thermal motions of atoms can be estimated from a calculated Hessian matrix, in work [P8] this parameter was used to show how far the effect of a defect manifests itself. Anisotropic displacement parameters (ADP) at a given temperature are calculated as 3 × 3 tensors UA associated with each atom in the A cell. Every 3 × 3 atomic tensor UA can be diagonalized as $U_A E_A = e_A E_A$, where e_A is the diagonal matrix of eigenvalues. If the three eigenvalues are positive, then the constant probability surfaces are ellipsoids, which include the probability of finding a given atom location. The lengths of the major axes

of the ellipsoids are proportional to the U_A eigenvalues e_1, e_2 and e_3, which are usually expressed as 10^{-4} A^2 [75].

3.3.2. Model and calculation parameters selection

In order to find a suitable calculation scheme, at the beginning of the work, calculations were performed with various functionals, using the smallest possible basis sets (Al – effective nuclear pseudopotential with valence $3s^23p^1$ electrons, O – 6*s*–2111*sp*–1*d* [63]), for the purpose of saving resources. The results of the calculations are listed in Table 3.1. Based on these results, the B3PW functional was chosen, which was used for most of the calculations. As available computing resources increased, the aluminum base set was replaced by the larger 8*s*–511*sp*–1*d*. For $MgAl_2O_4$ calculations, the same calculation parameters are used with the magnesium 8*s*–511*sp* basis set [63].

For the work on the vibrational properties of defects, it was separately tested how well the vibrational properties of an ideal crystal are reproduced (Table 3.2).

Table 3.1. Lattice parameters *a* and *c*, band gap and elastic constant for perfect corundum calculated using different exchange-correlation functionals. [P1]

Method (functional)	***a*, Å**	**Δ*a*,* %**	***c*, Å**	**Δ*c*,* %**	**Band gap ε_g, eV**	**$\Delta\varepsilon_g$,* %**	**Elastic constants, GPa [19]**			
							C_{11}	**Δ,* %**	C_{44}	**Δ,* %**
Experimental	4.76 [16]		12.99 [16]		8.8 [17]		496.5		146.2	
B3PW	4.775	0.32	12.979	–0.02	8.39	–4.7	494.2	–0.5	146.4	0.2
B3LYP	4.792	0.67	13.036	0.41	8.55	–2.8	488.4	–1.6	139.5	–4.5
HSE-sol	4.744	–0.35	12.884	–0.75	8.25	–6.3	516.8	4.1	150.2	2.8
PBE	4.788	0.59	12.987	0.04	6.01	–31	469.5	–5.4	142.3	–2.6

*as compared to experimentally found values written in previous columns

Table 3.2. Calculated and experimental Raman and IR modes of perfect α–Al_2O_3. Mode symmetry is given in parenthesis. [P8]

Raman, cm–1		**IR, cm–1**	
Calc.	**Experimental**	**Calc.**	**Exp.**
This work	Ref. [76]	This work	Ref. [77]
378 (E_g)	376	382 (E_u)	385
412 (A_{1g})	413	393 (A_{2u})	400
421 (E_g)	428	436 (E_u)	442
451 (E_g)	440	560 (E_u)	569
576 (E_g)	573	575 (A_{2u})	583
643 (A_{1g})	642	635 (E_u)	635
752 (E_g)	748		

4. MAIN RESULTS

4.1. Oxygen interstitial defects structure and properties

The first step in this work was to determine the structure of the neutral oxygen interstitial defect [P1, A1]. Later, other charge states were also explored: –1, 0, +1. It was concluded that in all cases the interstitial oxygen (O_i) occupies a position next to the regular oxygen atom (O_{reg}) (Fig. 4.1).

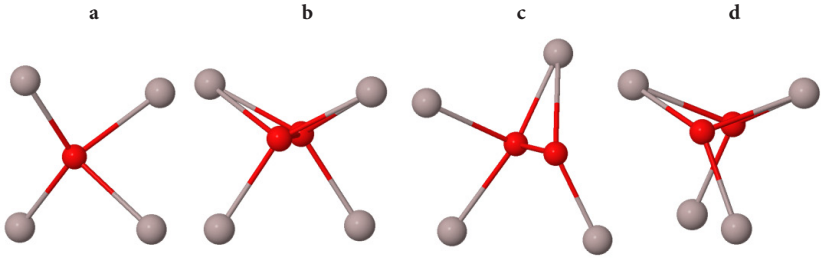

Figure 4.1. Oxygen site in α–Al_2O_3 lattice: a) without defect (O_{reg}), b) neutral interstitial oxygen defect, c) positively charged and d) negatively charged.

Table 4.1. Basic properties of the interstitial oxygen defect in different charge states in α–Al_2O_3 crystals.

Defect	O_{reg}	O_2^{2-} (q = 0)	O_2^{-} (q = +1)	$O_2^{\text{“3–“}}$ (q = –1)
Charge, e	–1.38	–0.74 / –0.74	–0.27 / –0.66	–1.05 / –1.05
$d_{O–O}$, Å	–	1.44	1.33	1.87
$d_{O–Al}$, Å	1.86, 1.97	1.85, 1.92	1.76 / 1.89, 2.04, 2.05	1.84, 1.85
Vibrational frequency, cm^{-1}	–	1069	1183	963

Looking at the properties of all defects, it can be concluded that some of them have a lot in common with the oxygen peroxide O_2^{2-} and superoxide O_2^{-} forms [78]. This can be inferred from both bond lengths and vibrational frequencies. A positively charged defect is also distinguished by the fact that in its case O_i and O_{reg} are not equal and symmetrical. The symmetric form was also modelled, but its energy was 0.2 eV higher. A negatively charged defect differs from the others with a longer bond length, which is not typical for widely known oxygen bond forms, but resembles the form of oxygen in the high–pressure FeO_2 bond, where the O_2^{3-} ion formally exists and the O–O bond is 1.937 Å [79].

The electron density distribution was analyzed using the electron localization function and the Laplacian of the electron density (Fig. 4.2). Electron localization function is a measure of probability of finding an electron in the neighborhood space of a reference electron located at a given point and with the same spin, and the Laplacian of the electron density represents the structure of the atomic shell, which changed its shape as a result of covalent bond formation and hybridization [80]. In the case of neutral and positively charged defects, the total electron density between the two atoms can be seen very well, indicating the formation of a bond. A negatively charged defect does not create shared electron density, so it cannot be said that a molecule-type structure is formed, but two separate atoms that arrange themselves in the crystal lattice.

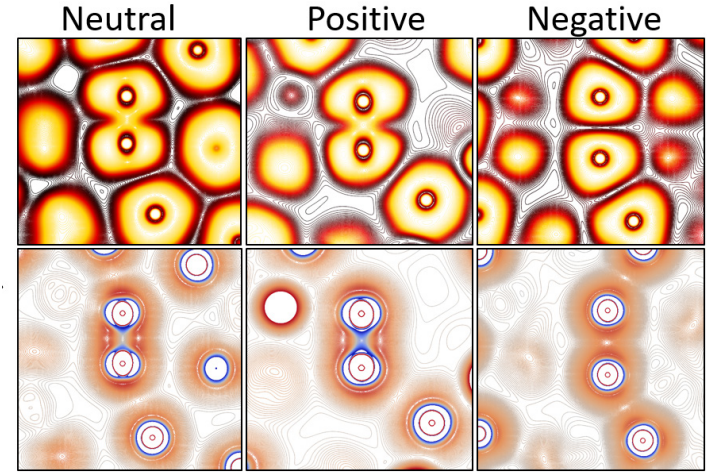

Figure 4.2. Interstitial oxygen defects in different charge states. 2D distribution of electron density using electron localization functions (top) and Laplacian of electron density (bottom).

The defect formation energy (Fig. 4.3) was calculated for all three charge states as a function of the Fermi energy, which is taken in the interval from the maximum of the valence band ($\varepsilon_{Fermi} = 0$) to the minimum of the conduction band. All three states are shown to have their own region of stability. O_2^- (q = +1) is more stable at lower Fermi energy, which is characteristic of hole-type defects. Two paramagnetic defects are expected to have smaller stability regions than diamagnetic O_2^{2-} (q = 0). This state was later also observed experimentally, where an absorption band at 6.53 eV was identified for this defect, while the defect in the q = +1 state forms an absorption band at 5.61 eV, and was also identified by the EPR technique [4, P8]. Meanwhile, the q = –1 state could play an important role in the defect recombination process, which will be discussed later.

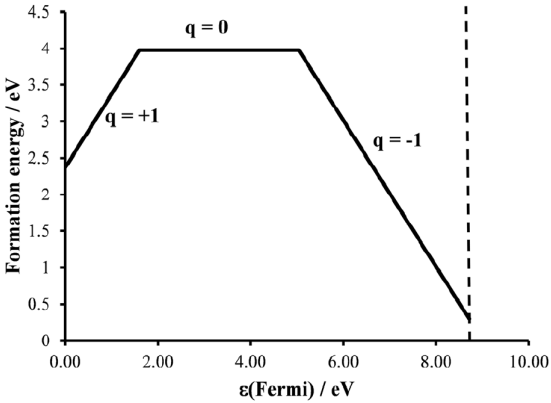

Figure 4.3. Formation energy of interstitial oxygen defects as a function of Fermi energy. Dashed line indicates the width of the band gap. [P8]

Only q = 0 and q = –1 states were considered in $MgAl_2O_4$ crystals. The properties of the defects in the two compounds are very similar, both in terms of bond lengths and charge distribution. As an example, we can look at the density state diagrams for defects in both crystals (Fig. 4.4). Both α–Al_2O_3 and $MgAl_2O_4$ neutral (q = 0) defects form occupied states immediately around the top of the valence band and unoccupied ones 8 eV higher. For negative defects, the diagram is slightly different, but in general their characteristics are also very similar.

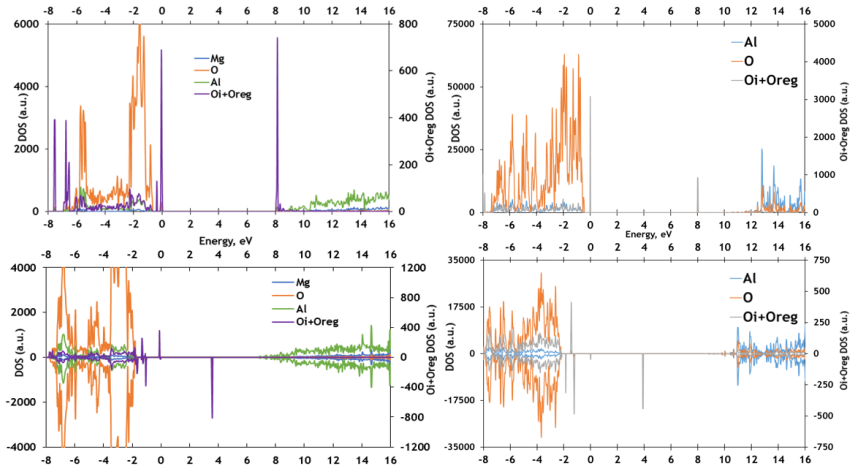

Figure 4.4. Density of states diagram of $MgAl_2O_4$ (left) and α–Al_2O_3 (right) with neutral (top) and negatively charged (bottom) oxygen interstitial defects. O_i+O_{reg} DOS shows the states introduced by oxygen defects, O – states of regular oxygen ions [P7]

4.2. Migration of oxygen interstitial defects in the crystal lattice

4.2.1. a–Al_2O_3

After determining the structure of the oxygen interstitial defect, the migration of this defect in the crystal lattice can be modelled. The defect was assumed to move through the lattice in a stepwise manner, with each step occupying a ground state.

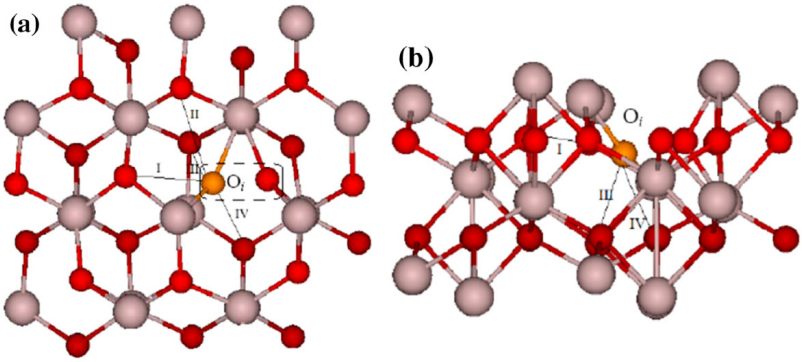

Figure 4.5. Four possible migration paths of the neutral interstitial oxygen atom in the α–Al2O3 lattice, top (0001) (a) and edge (b) views. Trajectories show the direction of a migration. Paths I and II are "in-plane" and III and IV – inter-plane. [P2]

The directions towards the nearest oxygen atoms were chosen as trajectories (Fig. 4.5.). Trajectories I and II start and end on the same (0001) plane, while trajectories III and IV pass between the two nearest planes. The initial migration jump lengths change in the following order: $d_I < d_{III} < d_{II} < d_{IV}$.

Three of the four energy curves, which were obtained using Distinguished Reaction Coordinate" (DRC), shown in Figure 4.6 cross a single barrier, while energy curve IV is characterized by a double-barrier profile, where the first barrier is associated with a 90-degree rotation of the Oi–Oreg structure, followed by single bond breaking and new bond formation. The calculated value of the migration barrier is ~1.3 eV, which is practically the same for three of the four trajectories. This value is very similar to that calculated for the case of MgO. But the calculated barrier is larger than it is observed in experiments – 0.2–0.9 eV, depending on irradiation conditions and dose [22]. Therefore, another model had to be considered.

Taking into account the properties of the oxygen interstitial defect in different charge states and experimental observations, O_i q = –1 defect migration was modelled next. From the analysis of the electron density, it could be concluded that in this state the O–O bond is the weakest, therefore the migration barrier should be lower.

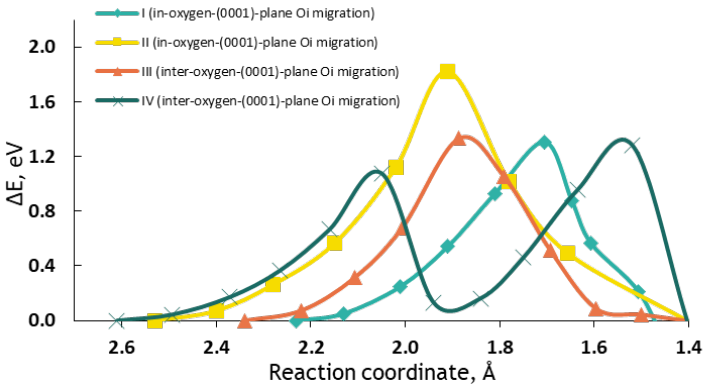

Figure 4.6. Reaction coordinate diagram for four interstitial oxygen atom migration paths in corundum I, II, III and IV (Fig. 4.5.) and calculated energy barriers. [P2]

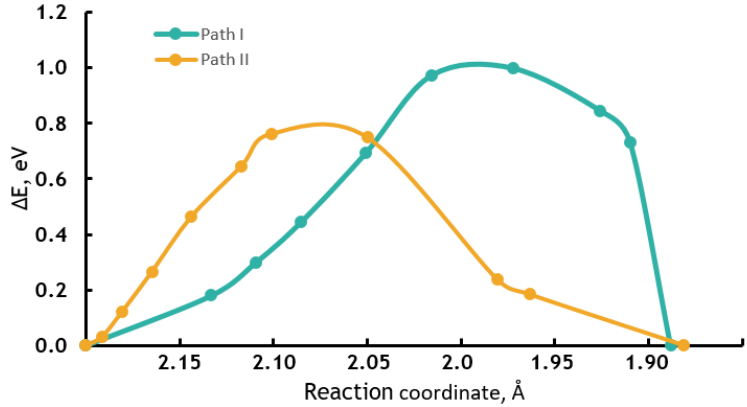

Figure 4.7. Reaction coordinate diagram for two negatively charged interstitial oxygen atom migration pathways and calculated energy barriers. [P6]

Four trajectories were considered in the work [P6]. But we managed to successfully model only two, which are shown in Figure 4.7. Difficulties in the calculations are mainly due to the fact that the extra electron during the migration cannot be localized so easily, and due to the larger initial O–O distance, the O_i atom in some trajectories is very close to other ions during the migration. The calculated barrier value is ~0.8 eV, which is in good agreement with experimental observations.

4.2.2. $MgAl_2O_4$

In the case of spinel, the migration of two types of defects was also examined. For a neutral defect, migration paths and calculated energy curves are shown in Figure 4.8. The three regular oxygen atoms closest to O_i (up to 2.5 Å away) were chosen as the final position for migration. The migration paths can be characterized as one-dimensional migration: path I lies in the <100> direction, paths II and III are oriented in the <110> direction. All pathways reveal a clear energy barrier and end in the formation of a new O–O pair with the regular oxygen atom

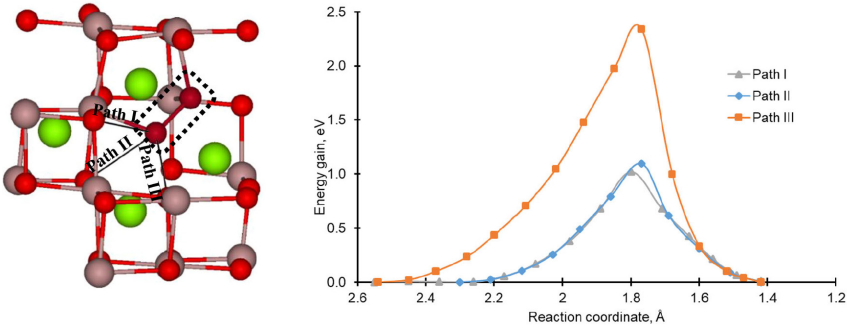

Figure 4.8. Left: fragment of a 113-atom supercell with three neutral Oi migration paths in a spinel crystal. Right: reaction coordinate diagram for three migration pathways and calculated energy barriers. [P7]

The calculated barriers are between 1.0 and 2.4 eV. A closer look at the peak point of trajectory III clearly shows that the increase in the energy barrier occurs due to the strong interaction with the Mg ion. At the same time, the O–O bond lengths and electronic structure are very similar for trajectories I and II. The only difference is the interaction with the Mg ion instead of the Al ion. This effect could be particularly important in Mg-rich spinels, where antisite defects in Mg_{Al} are common, which can affect oxygen migration.

Migration barriers are smaller than calculated for neutral oxygen interstitials in corundum (1.3 eV) and MgO (1.45 eV). If we assume that the limiting step for the migration of neutral oxygen interstitials is the breaking of the O–O bond, it can be concluded that an asymmetric environment in spinel could reduce the energy of this bond.

Unlike neutral O_i, the negatively charged O_i ion in spinel symmetrically occupies a regular oxygen site: each of two oxygen atoms forms covalent bonds with 2 Al atoms and one ionic bond with a Mg atom. There are two symmetric non-equivalent migration paths for the migration of interstitials between the nearest oxygen atoms (Fig. 4.9.).

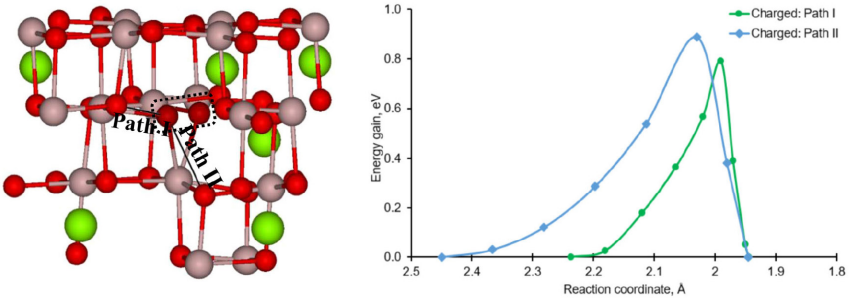

Figure 4.9. Left: fragment of a 113-atom supercell with two migration paths of negatively charged O_i in a spinel crystal. Right: energy curves for two migration pathways and calculated energy barriers. [P7]

Similar to the migration of a neutral O_i atom, trajectory I is oriented in the <100> direction and trajectory II along <110>. The calculated migration paths show lower energy barriers of 0.8–0.9 eV than for neutral Oi. Unfortunately, no experimental data on the recombination of oxygen defects in spinel crystals were found during the work.

4.3. $MgAl_2O_4$ antisite defects properties and EPR parameters calculations

A series of EPR active defects were calculated for spinel crystals, which were experimentally observed [49]: $V_1(=V_{Al}^{2-} + O^-)$, $V_2(=V_{Mg}^{1-} + O^-)$ and $V_{22}(=Mg_{Al}^{0} + O^-)$. Next to each defect is an O^- with a localized hole that produces an EPR signal. The spin density distribution is shown in Figure 4.10, where you can clearly see the localization of the hole and the oxygen ion, and a small spin density on neighboring oxygen ions.

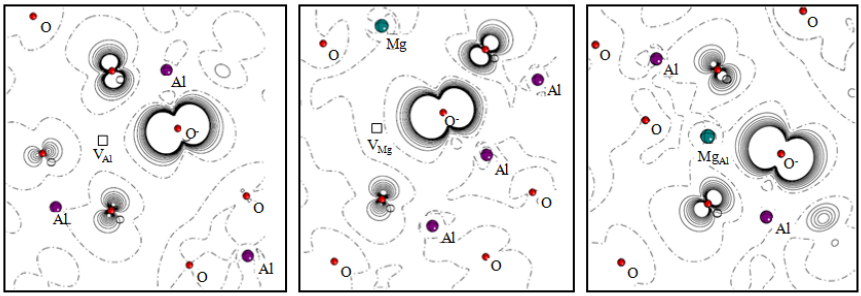

Figure 4.10. 2D spin density maps of V_{Al}, V_{Mg} and Mg_{Al} defects.

The calculated EPR parameters (Table 4.2) show nearly identical components of the Hyperfine Structure (HFS) tensor discussed [49], and are confirmed here for all three cases of V-centers despite the low symmetry. It should be noted that the centers of V_1 and V_{22} were calculated without symmetry constraints. While the relative calculation error may seem large, the absolute difference of 0.2 mT is small and within the accuracy of the calculation method.

Table 4.2. Calculated HFS parameters for V defects in spinel. Experimental values [49] are given in parentheses HFS parametres refers to aluminum ions adjacent to O^-.

Defect	A_{iso} / mT	A_x / mT	A_y / mT	A_z / mT
V_1	–0.60	–0.63 (0.86)	–0.65 (0.86)	–0.68 (0.93)
V_2	–0.71	–0.72	–0.71	–0.60
V_{22}	–0.58	–0.62 (0.45)	–0.60 (0.45)	–0.63 (0.46)

We calculated the formation energies (Fig. 4.11.) for vacancies and antisite defects in different charge states. V_1 center corresponds to aluminum vacancy in –2 charge state formation, V_2 center is Mg vacancy in charge state –1, and neutral Mg_{Al} antisite defect is V_{22} center. As expected, cation vacancies have the lowest formation energies in the highest charge states. The overall picture shows that the formation energies of the two cations are close in the corresponding charge states. Only the appearance of the –3 charge state of the Al vacancy makes this vacancy more energetically favorable compared to the –2 charge state of the Mg vacancy. However, the formation of an antisite defect is always the most advantageous, but it does not exclude the formation of other defects.

, we do not observe significant expansion
e in contrast to [24].
in density maps, oxygen atoms on larger
o not contain the holes. So, this part of the
ghbours of O^- is not delocalized over a
ocalize on them. In Table 3 we present
ıental values from [1] for a comparison.
the hyperfine coupling tensor were dis-
ed here for all the three cases of V-centres
percells. It indicated independence of the
gnetic field. Notice that the V_1 and V_{22}-
he supercells without imposing the sym-
ɔic contribution A^{iso} should be larger than
ɔle interaction B [19]. However, we

/-centres in $MgAl_2O_4$. *Q* and *M* the effective
moment of oxygen ion with the localized

Q/e	*M*/μ_B
–0.92	0.78

favourable in comparison with the Mg vacancy with the charge state –2. However, our main interest lies in the O^- ion (i.e. a single hole

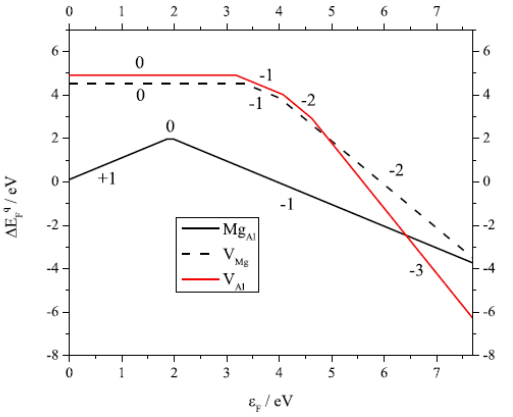

Figure 4.11. Formation energies of V_{Al}, V_{Mg} and Mg_{Al} defects as a function of Fermi energy.

4.4. Vibrational modes induced by point defects in α–Al_2O_3 crystals

In the last stage of the work, the vibrational properties of F-centers in α–Al_2O_3 crystals were examined. Compared to interstitial defects, the structure of F-centers is much simpler (Fig. 4.12), but the identification of induced vibration modes is more complicated. In total, two defects in three charge states were considered, all of them have been observed experimentally by optical methods [32].

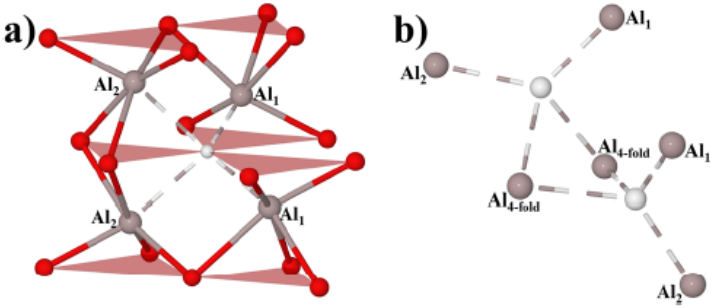

Figure 4.12. Schematic representation of F (a) and F_2 (b) centers in the α–Al_2O_3 structure. Al_1 and Al_2 are at different distances from the defect.

The results of the work [P8] on defect characteristics are summarized in Table 4.3.

Table 4.3. Calculated distances from the vacancy site to the nearest Al atoms (d_{V-Alx}, Å), Al–O bond length intervals for Al atoms around the vacancy (d_{Alx-O}, Å), charge (q, |e|) and magnetic moment (μ, μ_B), which is localized in the vacancy according to the results of the Mulliken analysis. Defect modes (cm^{-1}) were assigned by isotopic substitution analysis.

Defect	d_{V-Alx}	d_{Alx-O}	q	μ	Defect modes
F	Al_1: 1.75	Al_1: 1.88–2.10	1.46	0	146, 181, 231, 234, 252, 518
	Al_2: 2.01	Al_2: 1.85–1.97			
F^+	Al1: 1.98	Al_1: 1.85–1.96	0.87	0.66	214, 246, 248, 257, 830, 839
	Al2: 2.10	Al_2: 1.80–1.98			
F^{2+}	Al1: 2.17	Al_1: 1.79–1.95	0.25	0	714, 721, 848, 873, 891, 896
	Al2: 2.17	Al_2: 1.76–1.99			
F_2	Al1: 1.75	Al_1: 1.88–2.09	2.93	0	179, 231, 233, 238, 251, 335, 482
	Al2: 1.81	Al_2: 1.87–2.04			
		Al_{4-fold}: 1.86–1.97			
F_2^+	Al1: 1.90	Al_1: 1.85–1.96	2.3	0.68	184, 241, 243, 253, 337, 543
	Al2: 1.97	Al_2: 1.85–1.95			
		Al_{4-fold}: 1.84–1.97			
F_2^{2+}	Al1: 2.01	Al_1: 1.84–1.96	1.64	0	123, 184, 242, 250, 255, 835
	Al2: 2.11	Al_2: 1.83–1.98			
		Al_{4-fold}: 1.78–1.91			

First, the relaxation of atoms around the defects was analyzed. Similar trends were observed for the relaxation of mono– and dimer defects. Isotope substitution analysis was used to identify defect modes among several other modes (the calculation was performed in a 270–atom supercell without symmetry operators). All aluminum atoms (^{27}Al) around the defects were replaced by heavier ^{29}Al. This causes the frequencies of all modes associated with these atoms to be shifted to lower values (equation 3.2). From all the results, the F^{2+} defect, whose induced modes are in the region of 700–900 cm–1, stands out. To explain this, the anisotropic displacement parameters (ADP) of atoms were examined (Fig. 4.13).

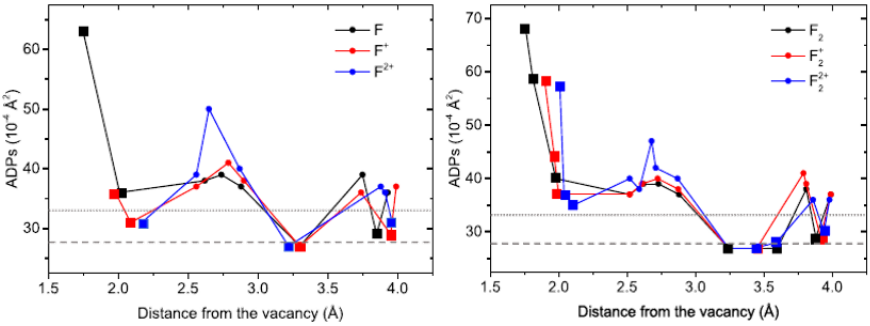

Figure 4.13. Anisotropic displacement parameters (ADP) for aluminum (squares) and oxygen (circles) atoms around defects. Horizontal dashed and dotted lines represent isotropic displacement parameters for aluminum and oxygen in an ideal crystal.

In ideal corundum, the ADPs of oxygen and aluminum are nearly isotropic, with little elongation along the *z* axis. The ellipsoids were found to be strongly anisotropic along the defect direction, here the maximum values of the three semi-axes of the thermal ellipsoids are visualized as a function of the distance of the oxygen and aluminum atoms from the vacancy. As expected, in the case of the F-center, the two Al atoms closest to the vacancy have an ADP almost three times larger than in the ideal crystal, while the other two Al atoms have a much smaller thermal ellipsoid, similar to the aluminum atoms at F^+ and F^{2+} defects. The second interesting observation revealed by studying ADP is the thermal motion of oxygen atoms in the second coordination sphere (distance 2.4 Å) of the F^{2+} center defect: here they have much larger ellipsoids than in other defects. The ADP analysis is consistent with the above considerations regarding changes in Al–O bonds. Induced modes in the low-frequency region for the F-center are associated with a shorter Al-vacancy distance (and thus longer Al–O bonds). On the contrary, induced modes in the high-frequency region (700–900 cm^{-1}) for the F^{2+}-center are associated with longer Al-vacancy distances and the involvement of oxygen atoms in thermal motion due to shorter Al–O bonds.

5. SUMMARY

This thesis is a systematic study of point defects in oxide materials α–Al_2O_3 and $MgAl_2O_4$, where special attention is paid to oxygen defects and related processes. The chosen method – hybrid DFT with LCAO approach – was tested for several basic parameters, such as lattice parameters, elastic modulus, and vibrational frequencies. The calculation results are in good agreement with the experimental results obtained during the work within the EUROfusion projects. An efficient comparison of calculation and experimental results allowed a deeper understanding of the behavior of Al_2O_3 and $MgAl_2O_4$ point defects, which can also be applied to the entire range of oxide materials.

For the first time stable configurations of the interstitial oxygen defect in –1/0/+1 charge states in Al_2O_3 crystals were determined. From the results of the defect migration modeling, it is concluded that the defect migration occurs in the 0 or –1 state. While in the ground state, the defect is most likely to exist in the +1 and 0 states, as shown by the experimental data. From this it can be concluded that the activation of defects occurs by electron capture.

Very similar results were obtained for $MgAl_2O_4$ crystals. Unfortunately, good experimental data on oxygen migration in these crystals are not yet available. The calculated electronic properties, structure and EPR parameters of EPR active defects are in good agreement with experimental data.

Vacancy defects in Al_2O_3 crystals have their own characteristic vibrational modes that could be observed by vibrational spectroscopy methods. Especially when radiation-induced defects are present at high concentrations and optical methods are no longer useful due to absorption saturation.

All work results have been systematized and published. They were used to explain and confirm the experimental results. The methods used in the work can be applied in the research of radiation properties in other materials as well.

6. MAIN THESES

The chosen approach for *ab initio* calculations of corundum and magnesium aluminate spinel was tested by a comparison of basic bulk properties with available experimental and theoretical data

- Oxygen interstitial defects in α–Al_2O_3 and $MgAl_2O_4$ are stable in neutral, positively charged or negatively charged state depending on experimental conditions. Interstitial defect migration occurs in a negatively charged form.
- V–centers associated with antisite defects or cation vacancies in $MgAl_2O_4$ crystals and localized holes on oxygen ions generate different EPR signals that can be distinguished and identified through *ab initio* calculation.
- All oxygen defects in α-Al_2O_3 crystals have their own characteristic and well–distinguishable vibrational modes, which could be observed by Raman spectroscopy methods. The vibration frequencies of the modes depend on the defect charge.

7. LITERATURE

7.1. Author's publications related to this work

[P1] **Platonenko, A.**, Piskunov, S., Zhukovskii, Y. F., Kotomin, E. A., *Ab initio* simulations on Frenkel pairs of radiation defects in corundum, IOP Conference Series: Materials Science and Engineering, **77** (1) (2015): 012001. IF = 0.53

[P2] Zhukovskii, Y. F., **Platonenko, A.,** Piskunov, S., Kotomin, E. A., *Ab initio* simulations on migration paths of interstitial oxygen in corundum, Nuclear Instruments and Methods in Physics Research, Section B: Beam Interactions with Materials and Atoms, **374** (2016): 29–34. IF = 1.27

[P3] **Platonenko, A.,** Gryaznov, D., Piskunov, S., Zhukovskii, Y. F., Kotomin, E. A., Charged oxygen interstitials in corundum: first principles simulations, Physica Status Solidi (C) Current Topics in Solid State Physics, **13** (10–12) (2016): 932–936. IF = 0.81

[P4] **Platonenko, A.,** Gryaznov, D., Zhukovskii, Y. F., Kotomin, E. A., *Ab initio* simulations on charged interstitial oxygen migration in corundum, Nuclear Instruments and Methods in Physics Research, Section B: Beam Interactions with Materials and Atoms, **435** (2018): 74–78. IF = 1.27

[P5] **Platonenko, A.,** Gryaznov, D., Zhukovskii, Y. F., Kotomin, E. A., First Principles Simulations on Migration Paths of Oxygen Interstitials in $MgAl_2O_4$, Physica Status Solidi (B) Basic Research, **256** (5) (2019): 1800282. IF = 1.48

[P6] **Platonenko, A.,** Gryaznov, D., Kotomin, E. A., Lushchik, A., Seeman, V., Popov, A. I., Hybrid density functional calculations of hyperfine coupling tensor for hole-type defects in $MgAl_2O_4$, Nuclear Instruments and Methods in Physics Research, Section B: Beam Interactions with Materials and Atoms, **464** (2020): 60–64. IF = 1.27

[P7] Seeman, V., Lushchik, A., Shablonin, E., Prieditis, G., Gryaznov, D., **Platonenko, A.,** Kotomin, E. A., Popov, A. I., Atomic, electronic and magnetic structure of an oxygen interstitial in neutron-irradiated Al2O3 single crystals, Scientific Reports, **10** (2020): 15852. IF = 4.58

[P8] **Platonenko, A.,** Gryaznov, D. Popov, A. I., Dovesi, R., Kotomin, E. A., First principles calculations of the vibrational properties of single and dimer F-type centers in corundum crystals, Journal of Chemical Physics, **153** (2020): 134107. IF = 2.99

7.2. Other author's publications

[A1] Evarestov, R. A., **Platonenko, A.,** Gryaznov, D., Zhukovskii, Y. F., Kotomin, E. A., First-principles calculations of oxygen interstitials in corundum: A site symmetry approach, Physical Chemistry Chemical Physics, **19** (37) (2017): 25245–25251. IF = 3.57

[A2] Evarestov, R. A., **Platonenko, A.**, Zhukovskii, Y. F., Site symmetry approach applied to the supercell model of $MgAl_2O_4$ spinel with oxygen interstitials: Ab initio calculations, Computational Materials Science, **150** (2018): 517–523. IF = 2.86

[A3] **Platonenko, A.**, Mackrodt, W. C., Dovesi, R., The Electronic Structures and Energies of the Lowest Excited States of the N_s^0, N_s^+, N_s^- and N_s–H Defects in Diamond, (2023) Materials, **16** (5), 1979

[A4] Usseinov, A., **Platonenko, A.**, Koishybayeva, Z., Akilbekov, A., Zdorovets, M., & Popov, A. I. Pair vacancy defects in β–Ga_2O_3 crystal: Ab initio study, (2022) *Optical Materials: **X***, 100200.

[A5] Mackrodt, W. C., **Platonenko, A.**, Dovesi, R., Self-trapped excitons in diamond: A Δ–SCF approach, (2022) *Journal of Chemical Physics*, **157** (8), 084707.

[A6] El-Kelany, K. E., Pascale, F., **Platonenko, A.**, Ferrari, A. M., Dovesi, R., Quantum mechanical simulation of various phases of KVF_3 perovskite (2022) *Journal of Physics Condensed Matter*, **34** (28), 285401.

[A7] Krasnenko, V., Rusevich, L. L., **Platonenko, A.**, Mastrikov, Y. A., Sokolov, M., Kotomin, E. A., Water Splitting on Multifaceted $SrTiO_3$ Nanocrystals: Calculations of Raman Vibrational Spectrum (2022) *Materials*, **15** (12), 4233.

[A8] Pascale, F., Doll, K., **Platonenko, A.**, Rérat, M., Dovesi, R., The role of spin density for understanding the superexchange mechanism in transition metal ionic compounds. The case of KMF3 (M = Mn, Fe, Co, Ni, Cu) perovskites (2022) *Physical Chemistry Chemical Physics*, **24** (21), pp. 12950–12960.

[A9] **Platonenko, A.**, Pascale, F., El-Kelany, K. E., Gentile, F. S., Dovesi, R., The effect of charge and spin state on the Infrared spectra and hyperfine coupling constants of point defects in Silicon (2022) *Physica B: Condensed Matter*, **626**, 413499.

[A10] Usseinov, A., Koishybayeva, Z., **Platonenko, A.**, Pankratov, V., Suchikova, Y., Akilbekov, A., Zdorovets, M., Purans, J., Popov, A. I., Vacancy defects in Ga_2O_3: First-principles calculations of electronic structure (2021) *Materials*, 14 (23), 7384.

[A11] Gentile, F. S., Diana, R., Panunzi, B., Caruso, U., **Platonenko, A.**, Pascale, F., Dovesi, R. Vibrational analysis of paraelectric–ferroelectric transition of linbo3: An ab-initio quantum mechanical treatment (2021) *Symmetry*, **13** (9), 1650.

[A12] **Platonenko, A.**, Colasuonno, F., Gentile, F. S., Pascale, F., Dovesi, R., Oxygen and vacancy defects in silicon. A quantum mechanical characterization through the IR and Raman spectra (2021) *Journal of Chemical Physics*, **154** (17), 174707.

[A13] **Platonenko, A.**, Gentile, F. S., Pascale, F., D'Arco, P., Dovesi, R., Interstitial carbon defects in silicon. A quantum mechanical characterization through the infrared and Raman spectra (2021) *Journal of Computational Chemistry*, 42 (12), pp. 806–817.

[A14] Usseinov, A., Koishybayeva, Z., **Platonenko, A.**, Akilbekov, A., Purans, J., Pankratov, V., Suchikova, Y., Popov, A. I., Ab-Initio Calculations of Oxygen Vacancy in Ga_2O_3 Crystals (2021) *Latvian Journal of Physics and Technical Sciences*, **58** (2), pp. 3–10.

[A15] Colasuonno, F., Gentile, F. S., Mackrodt, W., Ferrari, A. M., **Platonenko, A.**, Dovesi, R., Interstitial defects in diamond: A quantum mechanical simulation of their EPR constants and vibrational spectra (2020) *Journal of Chemical Physics*, **153** (2), 024119.

[A16] Di Palma, G., Kirtman, B., Gentile, F. S., **Platonenko, A.**, Ferrari, A. M., Dovesi, R., The VN_2 negatively charged defect in diamond. A quantum mechanical investigation of the EPR response (2020) *Carbon*, **159**, pp. 443–450.

[A17] Gentile, F. S., **Platonenko, A.**, El-Kelany, K. E., Rérat, M., D'Arco, P., Dovesi, R., Substitutional carbon defects in silicon: A quantum mechanical characterization

through the infrared and Raman spectra (2020) *Journal of Computational Chemistry*, **41**, 17, pp. 1638–1644.

[A18] **Platonenko, A.**, Popov, A. I., Structural and electronic properties of β–$NaYF_4$ and β–$NaYF_4$:Ce^{3+} (2020) *Optical Materials*, **99**, 109529.

[A19] **Platonenko, A.**, Gentile, F. S., Maul, J., Pascale, F., Kotomin, E. A., Dovesi, R., Nitrogen interstitial defects in silicon. A quantum mechanical investigation of the structural, electronic and vibrational properties (2019) *Materials Today Communications*, 21, 100616.

[A20] **Platonenko, A.**, Gentile, F. S., Pascale, F., Ferrari, A. M., D'Amore, M., Dovesi, R., Nitrogen substitutional defects in silicon. A quantum mechanical investigation of the structural, electronic and vibrational properties (2019) *Physical Chemistry Chemical Physics*, **21** (37), pp. 20939–20950.

[A21] **Platonenko, A.**, Piskunov, S., Bocharov, D., Zhukovskii, Y. F., Evarestov, R. A., Bellucci, S., First-principles calculations on Fe–Pt nanoclusters of various morphologies (2017) *Scientific Reports*, 7 (1), 10579.

[A22] Orola, L., Veidis, M. V., Sarcevica, I., Actins, A., Belyakov, S., **Platonenko, A.**, The effect of pH on polymorph formation of the pharmaceutically active compound tianeptine (2012) *International Journal of Pharmaceutics*, **432** (1–2), pp. 50–56.

7.3. References

1. Collaboration, Atlas. Combined search for the Standard Model Higgs boson using up to 4.9 fb–1 of pp collision data at sqrt(s) = 7 TeV with the ATLAS detector at the LHC. *Phys. Lett. B* **710** (2012): 49–66.
2. Collaboration, C. M. S. Combined results of searches for the Standard Model Higgs boson in pp collisions at sqrt(s) = 7 TeV. Phys. Lett. B **710** (2012): 26–48.
3. Chason, E., Ion beams in silicon processing and characterization. *Journal of Applied Physics* **81** (1997): 6513–6561.
4. Schulz-Ertner, Daniela, and Hirohiko Tsujii. Particle Radiation Therapy Using Proton and Heavier Ion Beams. *Journal of Clinical Oncology* **25** (2007): 953–964.
5. Stoneham, A., and R. Smoluchowski. Theory of Defects in Solids: Electronic Structure of Defects in Insulators and Semiconductors. *Physics Today* **29** (2001): 62–62.
6. Henderson, Brian. Anion vacancy centers in alkaline earth oxides. *Critical Reviews in Solid State and Materials Sciences* **9** (1980): 1–60.
7. Stuchbery, Andrew, and Eva Bezakova. Thermal-Spike Lifetime from Picosecond-Duration Preequilibrium Effects in Hyperfine Magnetic Fields Following Ion Implantation. *Physical Review Letters* **82** (1999): 3637–3640.
8. Kenik, E., and T. Mitchell. Orientation dependence of the threshold displacement energy in copper and vanadium. *Philosophical Magazine* **32** (1975): 815–831.
9. Nordlund, K., J. Wallenius, and L. Malerba. Molecular dynamics simulations of threshold displacement energies in Fe. *Nuclear Instruments and Methods in Physics Research Section B: Beam Interactions with Materials and Atoms* **246** (2006): 322–332.
10. Xiao, H., Threshold displacement energy in GaN:Ab initiomolecular dynamics study. *Journal of Applied Physics* **105** (2009): 123527.

11. Norgett, M., M. Robinson, and I. Torrens. A proposed method of calculating displacement dose rates. *Nuclear Engineering and Design* **33** (1975): 50–54.
12. Broom, T. Lattice defects and the electrical resistivity of metals. *Advances in Physics* **3** (1954): 26–83.
13. Nordlund, Kai, Primary radiation damage: A review of current understanding and models. *Journal of Nuclear Materials* 512 (2018): 450–479.
14. Zinkle, S., and C. Kinoshita. Defect production in ceramics. Journal of Nuclear Materials **251** (1997): 200–217.
15. Wendler, E., K. Gärtner, and W. Wesch. Comparison of ion-induced damage formation in and MgO. *Nuclear Instruments and Methods in Physics Research Section B: Beam Interactions with Materials and Atoms* **266** (2008): 2872–2876.
16. Hendricks, R., J. Schelten, and W. Schmatz. Studies of voids in neutron-irradiated aluminium single crystals: II. Small-angle neutron scattering. *Philosophical Magazine* **30** (1974): 819–837.
17. Mota, F., Ortiz, C. J., Vila, R., Casal, N., Garcia, A., & Ibarra, A., Calculation of damage function of Al_2O_3 in irradiation facilities for fusion reactor applications. *Journal of Nuclear Materials* **442** (2013): S699–S704.
18. Serikov, A., Bertalot, L., Clough, M., Fischer, U., & Suarez, A Neutronics analysis for ITER cable looms. *Fusion Engineering and Design* **96–97** (2015): 943–947.
19. Itoh, N., and K. Tanimura. Formation of interstitial-vacancy pairs by electronic excitation in pure ionic crystals. *Journal of Physics and Chemistry of Solids* **51** (1990): 717–735.
20. Lushchik, Ch, and A. Lushchik. Evolution of Anion and Cation Excitons in Alkali Halide Crystals. *Physics of the Solid State* **60** (2018): 1487–1505.
21. Zinkle, S., and L. Snead. Opportunities and limitations for ion beams in radiation effects studies: Bridging critical gaps between charged particle and neutron irradiations. *Scripta Materialia* **143** (2018): 154–160.
22. Popov, A. I. Lushchik, A., Shablonin, E., Vasil'chenko, E., Kotomin, E. A., Moskina, A. M., & Kuzovkov, V. N, Comparison of the F-type center thermal annealing in heavy-ion and neutron irradiated Al_2O_3 single crystals. *Nuclear Instruments and Methods in Physics Research Section B: Beam Interactions with Materials and Atoms* **433** (2018): 93–97.
23. Valbis, J., and N. Itoh. Electronic excitations, luminescence and lattice defect formation in α–Al_2O_3crystals. *Radiation Effects and Defects in Solids* **116** (1991): 171–189.
24. Stathopoulos, A., and G. Pells. Damage in the cation sublattice of α–Al_2O_3 irradiated in an HVEM. *Philosophical Magazine A* **47** (1983): 381–394.
25. Evans, B., A review of the optical properties of anion lattice vacancies, and electrical conduction in α–Al_2O_3: their relation to radiation-induced electrical degradation. *Journal of Nuclear Materials* **219** (1995): 202–223.
26. Averback, R., Ehrhart, P., Popov, A. I., and Sambeek, A. V., Defects in ion implanted and electron irradiated MgO and Al_2O_3. *Radiation Effects and Defects in Solids* **136** (1995): 169–173.
27. Lutterotti, L., and P. Scardi. Simultaneous structure and size\textendashstrain refinement by the Rietveld method. J. Appl. Crystallogr **23** (1990): 246.

28. Pells, G., and D. Philips. Radiation damage of α–Al2O3 in the HVEM. *Journal of Nuclear Materials* **80** (1979): 207.
29. Agnew, P. Displacement thresholds in sapphire. Philos. Mag. A **65** (1992): 355.
30. Evans, B., and Cain, L., A cation vacancy center in crystalline Al_2O_3. *Radiation Effects and Defects in Solids* **134** (1995): 329–332.
31. Evans, B., Pogatshnik, G., and Chen, Y., Optical properties of lattice defects in α–Al2O3. *Nuclear Instruments and Methods in Physics Research Section B: Beam Interactions with Materials and Atoms* **91** (1994): 258–262.
32. Shablonin, E., Popov, A. I., Prieditis, G., Vasil'chenko, E., and Lushchik, A., Thermal annealing and transformation of dimer F centers in neutron-irradiated Al_2O_3 single crystals. *Journal of Nuclear Materials* **543** (2021): 152600.
33. Popov, A. I., Lushchik, A., Shablonin, E., Vasil'chenko, E., Kotomin, E. A., Moskina, A. M., and Kuzovkov, V. N. Comparison of the F-type center thermal annealing in heavy-ion and neutron irradiated Al_2O_3 single crystals. *Nuclear Instruments and Methods in Physics Research Section B: Beam Interactions with Materials and Atoms* **433** (2018): 93–97.
34. Kotomin, E. A., Kuzovkov, V. N., Popov, A. I., and Vila, R., Kinetics of F center annealing and colloid formation in Al_2O_3. *Nuclear Instruments and Methods in Physics Research Section B: Beam Interactions with Materials and Atoms* **374** (2016): 107–110.
35. Kotomin, E., and A. Popov. Radiation-induced point defects in simple oxides. *Nuclear Instruments and Methods in Physics Research Section B: Beam Interactions with Materials and Atoms* **141** (1998): 1–15.
36. Hine, N. D. M., Frensch, K., Foulkes, W. M. C., and Finnis, M. W., Supercell size scaling of density functional theory formation energies of charged defects. *Physical Review B* **79** (2009): 24112.
37. Brudevoll, T., E. Kotomin, and N. Christensen. Interstitial-oxygen-atom diffusion in MgO. *Physical Review B* **53** (1996): 7731–7735.
38. Evarestov, R., P. Jacobs, and A. Leko. Oxygen interstitials in magnesium oxide: A band-model study. *Physical Review B* **54** (1996): 8969.
39. Sokol, A., A. Walsh, and C. Catlow. Oxygen interstitial structures in close-packed metal oxides. *Chemical Physics Letters* **492** (2010): 44.
40. Yuan, Y., Jiang, M., Zhao, F. A., Chen, H., Gao, H., Xiao, H. Y., Xiang, X. and Zu, X. T., Ab initio molecular dynamics simulation of low energy radiation responses of α–Al_2O_3. *Scientific Reports* **7** (2017): 1–11.
41. Halliburton, L., and L. Kappers. Radiation–induced oxygen interstitials in MgO. *Solid State Communications* **26** (1978): 111–114.
42. Hall, T. Studies of neutron irradiation damage in CaO. II. *Journal of Physics C: Solid State Physics* **9** (1975): 1369–1379.
43. Seeman, V., Reifman, S., Lehto, T., & Haldre, Ü., Family of O2− Centres in SrO Crystals. *physica status solidi (b)* **102** (1980): 459–465.
44. Lushchik, A., Kuzovkov, V. N., Kudryavtseva, I., Popov, A. I., Seeman, V., Shablonin, E., and Kotomin, E. A. The Two Types of Oxygen Interstitials in Neutron-Irradiated Corundum Single Crystals: Joint Experimental and Theoretical Study. *physica status solidi (b)* (2021): 2100317.

45. Lushchik, A., Kuzovkov, V. N., Kotomin, E. A., Prieditis, G., Seeman, V., Shablonin, E., Moskina, A., and Popov, A. I., Evidence for the formation of two types of oxygen interstitials in neutron-irradiated α–Al_2O_3 single crystals. *Scientific Reports* **11** (2021): 1–10.
46. Sickafus, K., Wills, J., and Grimes, N., Structure of Spinel. *Journal of American Ceramics Society* **82** (1999): 3279–3292.
47. Garner, F. A., Hollenberg, G. W., Hobbs, F. D., Ryan, J. L., Li, Z., Black, C. A., and Bradt, R. C., Dimensional stability, optical and elastic properties of $MgAl_2O_4$ spinel irradiated in FFTF to very high exposures. *Journal of Nuclear Materials* **212** (1994): 1087–1090.
48. Clinard, F., G. Hurley, and L. Hobbs. Neutron irradiation damage in MgO, Al2O3 and $MgAl_2O_4$ ceramics. *Journal of Nuclear Materials* **108** (1982): 655–670.
49. Lushchik, A., Dolgov, S., Feldbach, E., Pareja, R., Popov, A. I., Shablonin, E., and Seeman, V. Creation and thermal annealing of structural defects in neutron-irradiated $MgAl_2O_4$ single crystals. *Nuclear Instruments and Methods in Physics Research Section B: Beam Interactions with Materials and Atoms* **435** (2018): 31–37.
50. Ibarra, A., F. López, and Jiménez De Castro, M., V centers in $MgAl_2O_4$ spinels. *Physical Review B* 44.14 (1991): 7256–7262.
51. Lee, K., and J. Crawford. Electron centers in single-crystal Al_2O_3. *Physical Review B* **15** (1977): 4065–4070.
52. Uberuaga, B. P., Tang, M., Jiang, C., Valdez, J. A., Smith, R., Wang, Y., & Sickafus, K. E., Opposite correlations between cation disordering and amorphization resistance in spinels versus pyrochlores. *Nature Commun* **6** (2015): 8750.
53. Costantini, J. M., Lelong, G., Guillaumet, M., Weber, W. J., Takaki, S., & Yasuda, K., Color-center production and recovery in electron-irradiated magnesium aluminate spinel and ceria. *Journal of Physics: Condensed Matter* **28** (2016): 325901.
54. Gilbert, C. A., Smith, R., Kenny, S. D., Murphy, S. T., Grimes, R. W., & Ball, J. A., A theoretical study of intrinsic point defects and defect clusters in magnesium aluminate spinel. *Journal of Physics: Condensed Matter* **21** (2009): 275406.
55. Liu, C., Li, Y., Shi, T., Peng, Q., & Gao, F., Oxygen defects stabilize the crystal structure of MgAl2O4 spinel under irradiation. *Journal of Nuclear Materials* **527** (2019): 151830.
56. Ibarra, D., F. Bravo, and Lopez. V-centers in $MgAl_2O_4$ spinels. I. Sildos, *Materials Science Forum* **239** (1991): 595–598.
57. Ibarra, A., Vila, R., & De Castro, M. J., On the cation vacancy distribution in $MgAl_2O_4$ spinels. *Philosophical magazine letters* **64** (1991): 45–48.
58. Cain, L., G. Pogatshnik, and Y. Chen. Optical transitions in neutron-irradiated $MgAl_2O_4$ spinel crystals. *Physical Review B* **37** (1988): 2645–2652.
59. Summers, G. P., White, G. S., Lee, K. H., and Crawford Jr, J. H, Radiation damage in $MgAl_2O_4$. *Physical Review B* **21** (1980): 2578–2584.
60. Van Mourik, T., Bühl, M., & Gaigeot, M. P. . Density functional theory across chemistry, physics and biology. *Philosophical Transactions of the Royal Society A: Mathematical, Physical and Engineering Sciences* **372** (2011): 20120488.
61. Dovesi, R., Pascale, F., Civalleri, B., Doll, K., Harrisonet al., The CRYSTAL code, 1976–2020 and beyond, a long story. *The Journal of Chemical Physics* **152** (2020): 204111.

62. Erba, A., Baima, J., Bush, I., Orlando, R., and Dovesi, R., Large-Scale Condensed Matter DFT Simulations: Performance and Capabilities of the CRYSTAL Code. *Journal of Chemical Theory and Computation* **13** (2017): 5019–5027.
63. https://www.crystal.unito.it/basis-sets.php
64. Vilela Oliveira, D., Laun, J., Peintinger, M. F., and Bredow, T., BSSE-correction scheme for consistent gaussian basis sets of double- and triple-zeta valence with polarization quality for solid-state calculations. *Journal of Computational Chemistry* **40** (7 2019): 2364–2376.
65. Daga, L., Civalleri, B., and Maschio L., Gaussian Basis Sets for Crystalline Solids: All-Purpose Basis Set Libraries vs System-Specific Optimizations. *Journal of Chemical Theory and Computation* **16** (2020): 2192–2201.
66. Perdew, J., Burke, K., and Ernzerhof M., Generalized Gradient Approximation Made Simple. *Physical Review Letters* **77** (1996): 3865–3868.
67. Becke, A. Density-functional thermochemistry. III. The role of exact exchange. *The Journal of Chemical Physics* **98** (4 1993): 5648–5652.
68. Lee, C., Yang, W., and Parr, R., Development of the Colle-Salvetti correlation-energy formula into a functional of the electron density. *Physical Review B* **37** (1988): 785–789.
69. Grimme, Stefan, A consistent and accurate ab initio parametrization of density functional dispersion correction (DFT–D) for the 94 elements H–Pu. *The Journal of Chemical Physics* **132** (2010): 154104.
70. Makov, G., and M. Payne. Periodic boundary conditions inab initiocalculations. *Physical Review B* **51** (1995): 4014–4022.
71. Williams, Ian, and Gerald Maggiora. Use and abuse of the distinguished-coordinate method for transition-state structure searching. *Journal of Molecular Structure: THEOCHEM* **89** (10 1982): 365–378.
72. Friedland, E. Annealing of radiation damage in MgO single crystals after krypton implantation. *Nuclear Instruments and Methods in Physics Research Section B: Beam Interactions with Materials and Atoms* **85** (3 1994): 316–320.
73. Pascale, F., Zicovich-Wilson, C. M., López Gejo, F., Civalleri, B., Orlando, R., & Dovesi, R. The calculation of the vibrational frequencies of crystalline compounds and its implementation in the CRYSTAL code. *Journal of Computational Chemistry* **25** (2004): 888–897.
74. Zicovich-Wilson, C. M., Pascale, F., Roetti, C., Saunders, V. R., Orlando, R., & Dovesi, R., Calculation of the vibration frequencies of a-quartz: The effect of Hamiltonian and basis set. *Journal of Computational Chemistry* **25** (2004): 1873–1881.
75. Erba, A., Ferrabone, M., Orlando, R., & Dovesi, R., Accurate dynamical structure factors fromab initiolattice dynamics: The case of crystalline silicon. *Journal of Computational Chemistry* **34** (2013): 346–354.
76. Kadleíková, M., J. Breza, and M. Veselý. Raman spectra of synthetic sapphire. *Microelectronics Journal* **32** (12 2001): 955–958.
77. Marshall, R., Infrared Lattice Spectra of α–Al_2O_3 and Cr_2O_3. *The Journal of Chemical Physics* **43** (1965): 2893–2894.
78. Wiberg, E., Wiberg, N., and Holleman, A., *Inorganic Chemistry*. San Diego: Academic Press, (1996) p.1884

79. Hu, Q., Kim, D. Y., Yang, W., Yang, L., Meng, Y., Zhang, L., & Mao, H. K., FeO_2 and FeOOH under deep lower-mantle conditions and Earth's oxygen–hydrogen cycles. *Nature* **534** (2016): 241–244.
80. Cortesguzman, F., and R. Bader. Complementarity of QTAIM and MO theory in the study of bonding in donor-acceptor complexes. *Coordination Chemistry Reviews* **249** (2005): 633–662.

8. ACKNOWLEDGEMENTS

The author is grateful for the doctoral support from the ERDF project No. 8.2.2.0/20/I/006 "Strengthening the capacity of LU doctoral studies in the framework of the new doctoral model"

This work was carried out within the EUROfusion consortium and has received funding from the Euratom Research and Training Program 2014–2018 and 2019–2020 with agreement no. 633053, Enabling Research projects ENR-MFE19.ISSP-UL-02 "Advanced experimental and theoretical analysis of defect evolution and structural disordering in optical and dielectric materials for fusion application" and ENR-MAT.01.UT-T001-D001 "Investigation of defects and disorder in nonirradiated and irradiated Doped Diamond and Related Materials for fusion diagnostic applications (DDRM) – Theoretical and Experimental analysis". The views expressed here do not necessarily reflect the views of the European Commission.

The author is especially grateful to A. Popov for the much-needed support during my doctoral studies, involvement in experimental work and investments in my education and growth.

The author sincerely thanks all his co-authors for the experience, discussions and contribution to my growth.

The author is grateful to his supervisor D. Gryaznov for his help in completing the doctoral thesis.

The author is grateful to M. Putniņa and G. Zvejnieks for their help in polishing the work and suggested improvements.

The author is grateful to A. Lushchik from the University of Tartu for valuable discussions and introduction to experimental work on radiation defect studies.

Special thanks to Prof. R. Dovesi from the University of Turin for the time he devoted to me, introducing me to many great scientists and the very hospitable reception in Turin.

Calculations were performed on the ISSP cluster LASC, the HELIOS supercomputer (Japan), and the CINECA-MARCONI supercomputer (Italy).